Polymer Testing 145 (2025) 108757

Contents lists available at ScienceDirect

Polymer Testing

journal homepage: www.elsevier.com/locate/polytest

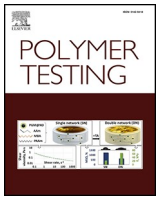

Synchronous application of DIC and DVC techniques for the global-local characterization of carbon fiber-reinforced composite laminates

Chaeyoung Hong [1], Minsu Park, Wooseok Ji [*]

Department of Mechanical Engineering, Ulsan National Institute of Science and Technology, Republic of Korea

ARTICLE INFO

Keywords:
Synchrotron radiation
Digital image correlation
Digital volume correlation
Multi-scale *in situ* tests

ABSTRACT

DIC is capable of continuously measuring the global deformation behavior of a specimen because its scanning can be done quickly over a wider observation area. While the DIC information is limited to the surface on which a speckle pattern is applied, DVC can compute three-dimensional strain fields inside a material. However, DVC data can be obtained over a smaller region at a limited number of load levels. Here, the DIC and DVC techniques are simultaneously utilized for the first time. The previous *in situ* test setup of the authors based on synchrotron radiation computed tomography was modified to add the DIC capability. The *in situ* testbed was installed with a CCD camera with blue lighting to obtain images for DIC analysis. The opaque tubular frame of a micro-tensile stage was newly fabricated with a transparent material causing minimal optical distortion. The qualities of speckle pattern images obtained through the transparent tube were carefully evaluated. The combination of the DVC and DIC techniques was demonstrated with an open-hole tensile test. The global and local failure progression of the composite was non-destructively characterized. Especially, a load-displacement curve without machine compliance was obtained because the deformation of the specimen could be directly measured owing to the DIC technique. The resolutions of DVC and DIC in the presented study were 0.65 μm and 2.27 μm, respectively. This specification is expected to provide unprecedented results that can truly validate multi-scale simulation models.

1. Introduction

X-ray computed tomography (CT) is a non-destructive inspection (NDI) method that is often used to visualize three-dimensional (3D) features inside hierarchically structured materials. A typical example of hierarchical materials is fiber-reinforced composites. The NDI technique has effectively evaluated the fiber architecture and/or defects inside the heterogeneous materials, across multiple length scales ranging from laminates and fiber bundles to individual fibers. Recently, many researchers have utilized X-ray CT to scan their specimens while mechanical testing is being performed [1–5,7–10,12–19]. The *in situ* testing methods have provided useful insight into mechanical behavior occurring inside the materials [1]. Especially when combined with a digital volume correlation (DVC) technique, the time-lapse X-ray CT becomes a powerful tool for identifying damage mechanisms based on the quantitative measurements of internal deforming behavior [2].

Despite the unprecedented benefits, there are still some issues limiting more practical use of the X-ray CT-based experimental method. Most critically, the size of a field of view (FOV) is substantially small, especially at high-magnification settings to identify micro-scale fibers in composite materials. Fibers should be recognizable in CT images because they are the natural speckle pattern for the DVC technique [5]. For carbon fibers, a physical pixel size of 1.6 μm or less is needed. An ideal pixel size for glass fibers is 3 μm or less. In addition, the detection of microscopic matrix cracks and mode II delamination requires a physical pixel size of 1.6 μm or less [6]. However, the spatial resolution has a trade-off relationship with the FOV size. When the spatial resolution of 1.625 μm is set on the Pohang Accelerator Laboratory (PAL) 6C BMI beamline, for example, the observation window size becomes 3.4125 mm × 2.765 mm [7]. FOVs of most studies visualizing carbon fibers in 3D space are constrained to the size of 1 mm–4 mm [8–13]. This small observation window requires specially designed specimens. Specimens should be made narrow to fit their widths into FOV [5]. In addition, double-notches [9,10,12,13] or a single-notch [14–16] were typically introduced to the specimens to locate FOV over the notched areas. In this manner, the onset of physically meaningful phenomena

* Corresponding author.
E-mail address: wsji@unist.ac.kr (W. Ji).
[1] Currently at Hyundai Motor Group

https://doi.org/10.1016/j.polymertesting.2025.108757
Received 8 December 2024; Received in revised form 15 February 2025; Accepted 6 March 2025
Available online 6 March 2025

can be captured within FOV. However, the results obtained within this small FOVs are often disconnected from the global response of composite materials.

Another problematic issue is the compliance of miniature tensile stages typically employed for synchrotron-based *in situ* tests. The frame of such loading devices is usually made in the form of a tube, instead of two parallel pillars [14,17–20]. The tubular frame encloses a sample and thus is made of X-ray penetrable materials such as polymethyl methacrylate (PMMA) [14,17,18], aluminum [19], or glassy carbon [20]. These materials also deform during a tensile test and the deformation may be siginficanlty included in the total displacement recorded by a tensile stage. Reliable global response data of a sample deformation only is critical to validate numerical models, but it is difficult to isolate the deformation associated with the tubular frame. This is probably why such a validation has not been attempted to the best of the authors' knowledge while various *in situ* test data are now available in the literature. Although the machine compliance could be isolated when the sample deformation is directly measured, it is technically impossible to install measuring instruments onto a specimen without interfering with the X-ray path.

A digital image correlation (DIC) technique is employed here to resolve the aforementioned issues of the current *in situ* test methods. DIC is capable of continuously measuring the global deformation behavior of a specimen because its scanning can be done quickly and cover a wider observation area. DIC analysis is expected to reliably provide a global stress-strain curve because a sample deformation can be directly measured. The global and local data obtained from the DIC and DVC techniques, respectively, will provide more detailed insight into the mechanical behavior of a composite material. In the presented study, we report on the simultaneous application of DIC and DVC techniques for the first time. DIC image acquisition system was established and added into our existing *in situ* test setup. The opaque tubular frame of a tensile stage was replaced with a transparent one. The validity and integrity of DIC patterns obtained through the transparent tube were examined. Subsequently, a multiscale experiment was conducted on a carbon fiber-reinforced composite specimen with an open hole.

2. Test materials and methods

2.1. Test specimen

The composite material system used in this study was the same as that used in Ref. [11]. A laminated composite panel with a $[90_2/0_2]_S$ stacking sequence was utilized. The laminated composite was fabricated using an autoclave process. The specimens were cut into an open-hole shape, as shown in Fig. 1. The panel was cut at a 45-degree angle using a water jet with a nozzle diameter of 0.6 mm. A hole was cut in the center of the specimen, and due to the V-shape taper effect of the water jet, the hole diameter was not uniform. CT inspection results showed no delamination caused by the hole machining.

2.2. Digital image correlation system with X-ray CT

2.2.1. Modified tube assembly

Fig. 2(a) shows the commercial loading device (Deben CT5000) available in the PAL 6C BMI beamline. The tube assembly of the tensile tester consists of top and bottom parts and a tube. The tube in Fig. 2(a) is made of opaque but X-ray penetrable glassy carbon for scanning a sample inside. However, for DIC analysis, a transparent tube is required for a camera to capture the surface images of a specimen. In this study, the opaque glassy carbon tube was replaced with the transparent quartz one, as shown in Fig. 2(b). The top and bottom parts of the tube assembly were also replaced with aluminum. The aluminum-based parts having the same dimensions as the original ones were manufactured through computer numerical control (CNC) machining. The dimensions were measured by a coordinate measuring machine (CMM).

Although the quartz material was selected for the tube here, PMMA was often used in other similar studies [14,17,18]. Indeed, we also considered the two materials for the transparency. The selection criteria for the material included optical transparency, mechanical stiffness and strength under compressive force, optical distortion, and market availability of pipes with the targeted diameter and thickness. As listed in Table 1, PMMA has relatively lower mechanical properties but is sufficiently strong to be used as a replacement tube. Moreover, PMMA is more cost-effective compared to quartz. However, PMMA critically induced optical distortion. The optical distortion was evaluated by comparing two images taken with and without the tube through the DIC technique. No mechanical loading was applied for this image identicalness test. Fig. 3 shows the DIC results of the PMMA and quartz tubes. The PMMA tube resulted in significant errors in the DIC results due to

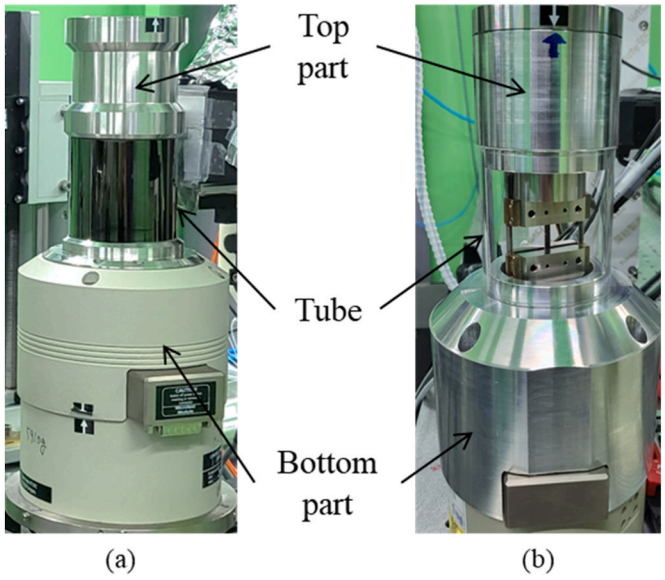

Fig. 2. Tube assembly (a) Existing part (b) Modified part.

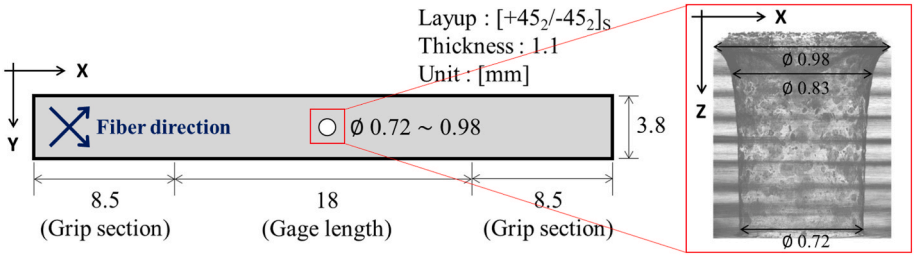

Fig. 1. Open-hole tension specimen.

Table 1
Properties of candidate materials for a transparent tube.

Features	PMMA	Quartz
Transmission rate	93 %	92 %
Compressive strength	85~110 MPa	490~1960 MPa
Young's Modulus	2.9 GPa	76.5 GPa
Optical distortion	Severe	Negligible

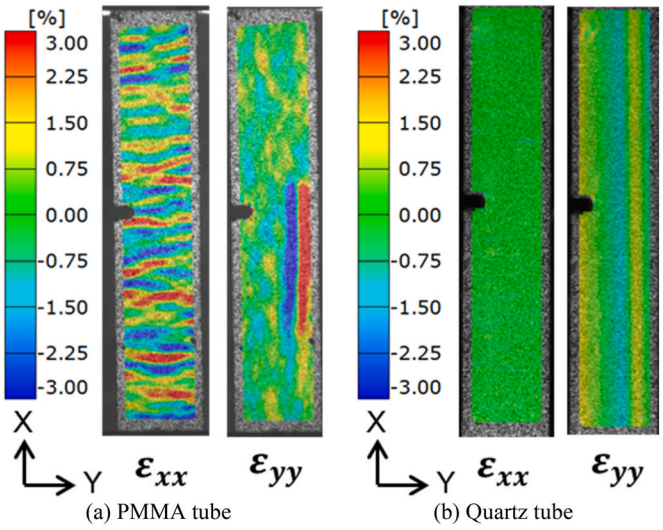

Fig. 3. DIC compares images with and without a tube.

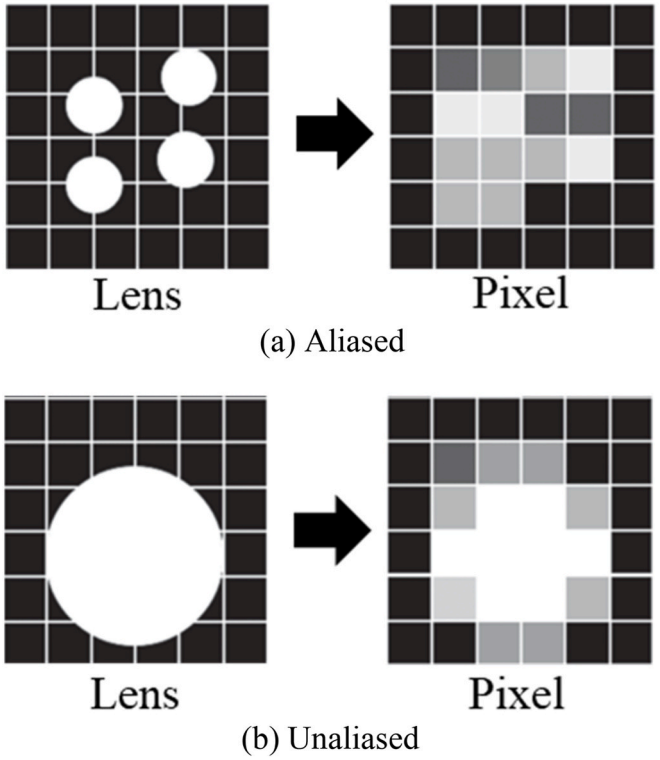

Fig. 4. Speckle pattern size.

partial distortions, imperceptible by human eyes. The quartz material, on the other hand, exhibited relatively low optical distortion and thus selected as a replacement of the opaque glassy carbon tube. However, the transverse strain in Fig. 3(b) was still erroneous compared to the axial strain. Therefore, only the axial strain was utilized in the presented study.

The quartz tube and parts were not bonded or joined but were held in place by the compressive force transmitted when tensile force is applied to a specimen. The outer and inner diameters of the quartz tube were set to 65 mm and 60 mm, respectively. In this case, the maximum stress in the tube would be 10 MPa at the maximum load capacity of the loading equipment (5 kN). 10 MPa is significantly lower than the maximum strength of the quartz material as listed in Table 1. Because of the higher X-ray absorption rate, the quartz tube requires six times longer exposure time than the glassy carbon tube.

2.2.2. *DIC speckle pattern*

The precision and accuracy of DIC analysis are highly dependent on a speckle pattern. The speckle pattern is typically created on a sample surface by first coating with white paint, followed by the application of black paint. According to the ARAMIS manual [22], the ideal speckle size should be more than five times the image pixel size but less than 15 pixels. In this experimental setup, the image pixel size is 2.27 μm. As shown in Fig. 4(a), if the pattern size is smaller than the recommended size, aliasing may occur because the speckles are indistinguishable at the pixel level. Fig. 4(b) shows an ideal speckle size that can be recognized in an image. However, too large speckle sizes may produce inaccurate strain calculations or require larger facets, which decreases strain resolution.

For generating an optimal speckle pattern, an airbrush gun was used. The sample surface was first sprayed with white paint, and then black paint dissolved in an organic solvent was applied using the airbrush gun to create a fine pattern. Fig. 5 shows the speckle pattern produced at various densities. The pattern size ranged from a minimum of 20 μm to a maximum of 60 μm. The pattern density was proportional to the paint application time. If pattern density is too low, black dots may not exist within a facet. On the other hand, in a high-density pattern, facets may lose their own uniqueness, leading to noise in strains. In this study, the pattern density shown in Fig. 5(b) was used.

Since the speckle pattern was repeatedly exposed to X-rays, any possible radiation effect on the paint was investigated. Fig. 6 shows the same speckle pattern exposed to synchrotron radiation for different periods. The beam intensity was set at 22 keV, and the beam current was 250 mA. As shown in Fig. 6, the paint was neither evaporated nor delaminated even after the 450-s exposure. The correlation values from the matching evaluation using images before and after the X-ray exposure were over 0.99. The correlation value can have a practical range of 0–1, wherein 1 implies that two comparing images are perfectly identical [21].

2.2.3. *Image acquisition system*

The image acquisition system consisted of a camera, lens, and lighting. A GigE interface-based CCD camera (GS3-PGE-60S6M – C, Teledyne FLIR) was used because it could be remotely controlled outside the beamline container room. The camera featured a 1-inch image sensor with a resolution of 2736 × 2192 pixels and a pixel size of 4.54 μm. The lens determined the size of the observation area and the image quality. A 2 × telecentric lens (VS-THV2-150/S, VS Technology) combined with the CCD camera resulted in an observation area size of 6.21 mm × 4.97 mm. Telecentric lenses are designed to minimize the perspective distortion of regular lenses, crucially deteriorating the accuracy of DIC calculations. In addition, telecentric lenses can provide sharper images without requiring a large depth of field. The working distance of the lens in the presented study was 150 mm. The distance provided a sufficient space between the sample and the DIC camera system and did not cause any interference with experimental equipment.

The lighting system included blue ring lighting, a brightness controller, and a 3-axis position adjustment system. Short-wavelength lighting, such as blue light, produced clearer images with less noise compared to white light due to reduced dispersion and distortion. It also

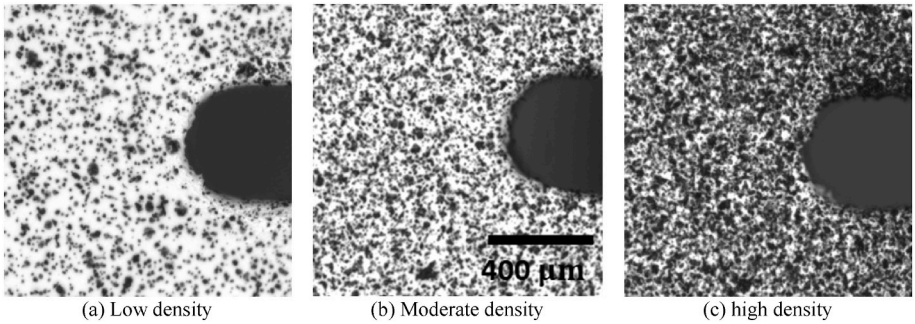

Fig. 5. Speckle pattern density.

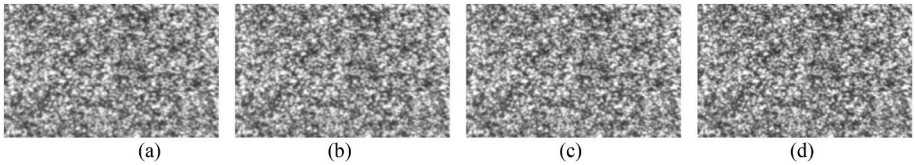

Fig. 6. Assessment of paint integrity for speckle pattern under synchrotron X-ray exposure. (a) Reference image (b) Image after 150-s exposure. Correlation value was 0.9968. (c) Image after 300-s exposure. Correlation value was 0.9952. (d) Image after 450-s exposure. Correlation value was 0.9918.

generated stronger illumination, which was beneficial for capturing fine details. The ring shape ensured uniform lighting across the sample, reducing shadow formation caused by slight height differences in the speckle pattern. The appropriate image brightness was determined by a combination of lens aperture settings, exposure time, and lighting brightness. The brightness controller was useful to achieve the optimal DIC settings. The 3-axis position adjustment system was used to find the lighting position that minimized specular reflections, which may cause DIC calculation failure.

2.3. Experimental setup for DIC and DVC

Fig. 7 shows the schematic and actual configuration of the combined DIC and DVC experiment. The DIC observation equipment was added to the existing *in situ* experiment setup of the authors [5,7,14,21]. The DIC system was installed in a position that did not interfere with the X-ray path. Tomography was performed at desired load levels. Once the tomography was complete, the precision rotation stage was activated to position the speckle-patterned sample surface to face the DIC system. Subsequently, loading continued to the next load level while DIC images were acquired. When the next load level was reached, the loading was halted, and another tomography scan was performed. By repeating this process, surface data of the specimen were obtained at all load intervals, and internal data of the specimen were acquired at specific load values. The loading was applied by a displacement control at the speed of 0.1 mm/min. Image acquisition began after the specimen was loaded approximately at 4.5 MPa.

Fig. 8 shows the specimen mounted on the modified loading device and the observation area sizes for DIC and DVC. Because the loading device was designed to fix the top of the specimen and pull down its

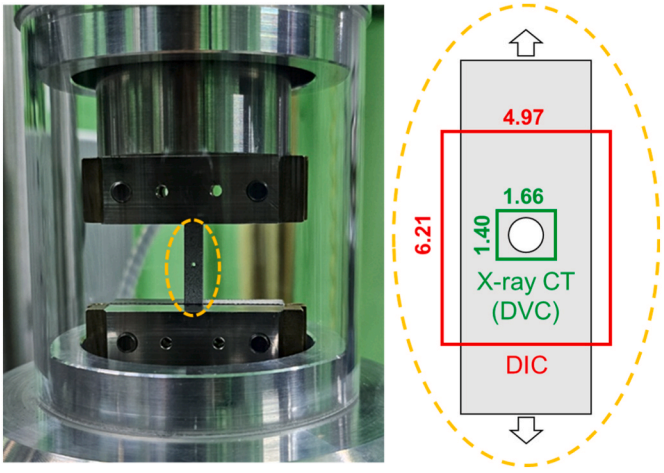

Fig. 8. FOV sizes for DIC and DVC analyses.

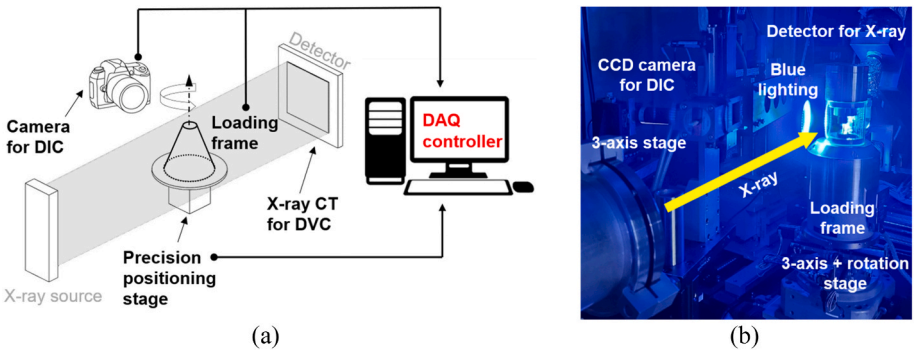

Fig. 7. (A) Schematic illustration of the DIC and DVC test setup (b) Actual test setup at the beamline 6C at PAL.

bottom to apply tension, the observation area was set so that the hole position was slightly above the center. Images for DIC analysis were acquired every second while the exposure time was set to 400 ms.

The X-ray image acquisition system was configured with a 10 × microscope lens and a PCO Edge 5.5 camera. The imaging system had a FOV size of 1.40 mm × 1.66 mm, as depicted in Fig. 8, with a pixel size of 0.65 μm. The FOV for the X-ray CT was set to closely observe the cracking and deforming behavior occurring at the edge of the hole. The beam energy and the beam current were set to 22 keV and 250 mA, respectively. The distance between the sample and the detector was 45 mm. The exposure time was set to 300 ms, taking into account the X-ray absorption of the quartz tube. A total of 2951 transmission images were recorded during a 180-degree rotation.

3. Results and discussion

3.1. Global stress-strain data

Fig. 9 shows the global stress-strain curve of the OHT specimen. The global stress-strain curve is crucial for this type of analysis because it serves as the synchronization basis for DIC, DVC, and CT results. The stress in Fig. 9 was calculated by dividing load data by the thickness and width of the specimen. The load data was recorded by the load cell installed in the loading frame. The maximum stress was 77 MPa. The DIC strain was defined as the rate of change in the average distance between facets located 2 mm above and below the hole center. The strain of the blue curve was calculated by dividing the crosshead displacement by the gauge length of the specimen.

As can be seen in Fig. 9, the two different strain measurements yielded significantly discrepant results, which is mainly caused by machine compliance. It is well known that a testing machine contributes to total measured displacement through the deformation of its load frame, grips, and fixtures when a load is applied. This unwanted contribution becomes more pronounced when a material as stiff as the machine is tested. However, the machine compliance can be effectively eliminated by directly measuring the deformation of a sample using strain gages, extensometers or the DIC technique. In Fig. 9, approximately at 0.28 % strain, the axial stiffnesses of the black and blue curves are 12.8 GPa and 9.3 GPa, respectively. The theoretical axial stiffness of a $[+45_2/-45_2]_S$ composite without a hole is 15.0 GPa, computed based on the classical laminate theory using the material properties of a single prepreg in Table 1 of [14]. Therefore, the DIC-based stress-strain curve was utilized as the synchronization basis for the following investigation. The red circles in Fig. 9 indicates the load levels when CT scans were performed.

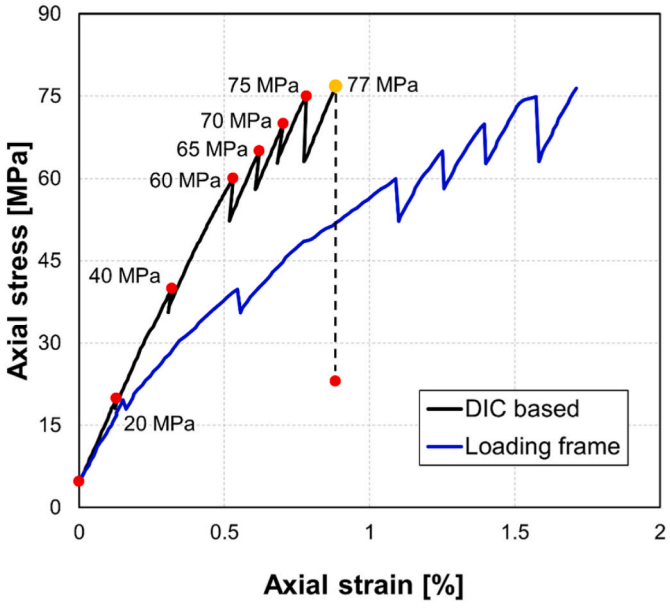

Fig. 9. Stress-strain response. Red dots indicate the load levels for X-ray CT scans.

3.2. DIC and DVC results

Fig. 10 shows the DIC results on the specimen surface at selected load levels. The DIC strains were calculated using ARAMIS 6.3 with a facet size of 19 and a step size of 15. It is noted here that DIC results were available at almost every load level in addition to the red points in Fig. 9 because the CCD camera captured images every second during the test. Thanks to the fine resolution, it was found that strain concentrations on both sides of the hole became prominent from the load level of 47 MPa, as shown in Fig. 10(b). Initially, the strain was concentrated along the fiber direction. However, from the load level of 57 MPa, the strain in the internal −45° layer was also reflected on the surface, revealing the X-shaped strain concentration pattern.

DVC results are displayed in Figs. 11 and 13. The DVC strains were calculated using an in-house MATLAB-based code [5,21]. The sub-volume size was 100 voxels, and the step size was 50 voxels. As illustrated in Fig. 11(a), strains in the mid-planes of each layer and interfaces could be obtained. The rectangle frame for the DVC results was defined in Fig. 8. Fig. 11(b) compares the internal in-plane strains at different positions and load levels. At the top of the hole, some erroneous DVC results were produced due to the locally poor quality of CT images. However, on both sides of the hole, highly concentrated strains were successfully captured. The strain concentration patterns manifested as the load increased. At 75 MPa, it was clearly seen that the strain patterns across the hole were slightly tilted counterclockwise and clockwise in the +45° and −45° layers, respectively. As a result, in the interface, highly concentrated strains were developed evenly on both sides of the hole. It is interesting to note that no X-shaped pattern were observed in the small DVC window.

In Fig. 13, strains around the hole are displayed in an unwrapped view. The strains were computed on a cylindrical surface of which the diameter is 10 % larger than that of the hole. The height and width in Fig. 13 represent the circumference of the hole and the thickness of the specimen, respectively. The circumferential and through-thickness positions are defined as illustrated in Fig. 12. The contour color in Fig. 13 displays tensile strain.

As shown in Fig. 13, two bands of strain concentration were found along the thickness direction: one in the 60°–120° range and the other in the 240°–300° range. The angle at which the maximum strain occurred varied slightly with the fiber orientation. In the +45° layer, strain concentration occurred at angles slightly greater than 90° and 270°, whereas in the −45° layer, it occurred at angles less than 90° and 270°. This trend became more pronounced as the load increased. The strain bands were continuous up to 97 % of the maximum stress level, implying no interfacial failure although the interfaces were highly strained as shown in Fig. 11(b). Indeed, no significant damage or failure was detected up to 75 MPa from tomographic images as will be discussed in the following section.

3.3. Tomography results

Tomography data were obtained at the red points in Fig. 9, but no damage or failure was found up to 70 MPa. Initial matrix cracks were detected only at 75 MPa, just before the peak load. At 77 MPa, marked as the yellow circle in Fig. 9, a sudden load drop occurred while the specimen was being scanned. CT scanning was thus conducted again at 26 MPa, and the final fracture patten in the specimen was acquired.

Fig. 14(a) shows the initial matrix crack found in 4-ply at 70 MPa. The crack was located between 270° and 300° by the angular position defined in Fig. 12, which lies within the strain concentration band. The initial crack seemed to be closed after the load drop as depicted in

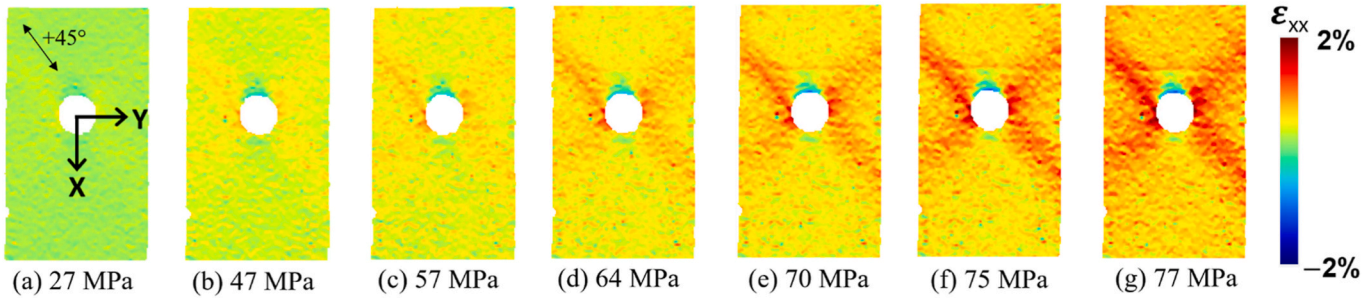

Fig. 10. DIC strain fields at various load levels.

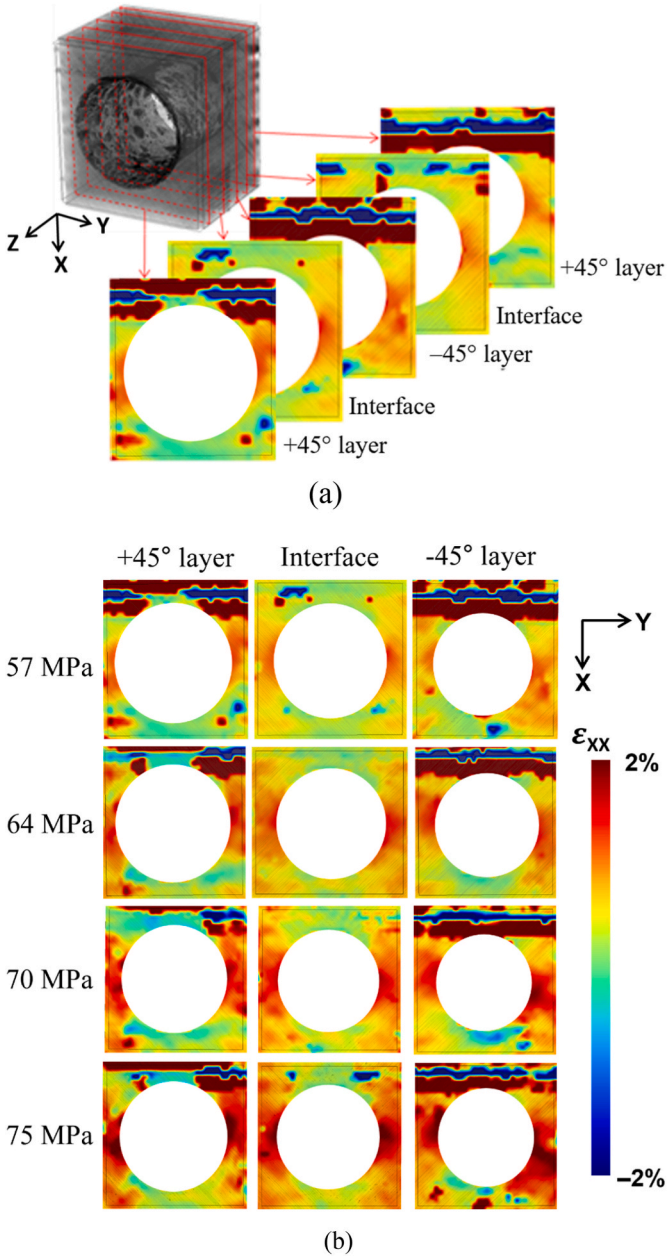

Fig. 11. Internal in-plane strains from DVC analysis.

Fig. 14(b). Fig. 15(a) displays the crack found in 8-ply. It was also located within the same strain concentration band. The crack spanned only half of 8-ply at 75 MPa, but, in the final stage, developed across

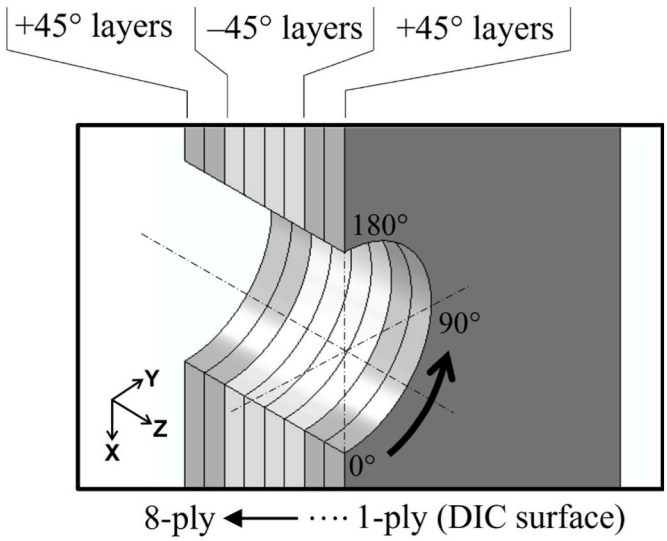

Fig. 12. Schematics of circumferential and through-thickness positions.

entire 8-ply. Near the fully-grown crack, a transverse crack propagated across 7-ply and 8-ply was found as shown in Fig. 15(b). It seems that the growth of the first crack in 8-ply was disturbed by the emergence of the major transverse crack. At the tip of the major transverse crack, delamination failure was observed. This implies that the delamination might be initiated by the transverse crack as explained in Ref. [11].

Indeed, delamination failure was not detected even at the peak load. Fig. 16(a) is the radiograph taken at the peak load before the sudden load drop occurred. No delamination was found except the matrix cracks indicated with the green arrows. Fig. 16 (b) and (c) are the projection images showing wide delamination areas at the interfaces after the peak. Therefore, it can be concluded that the delaminations were developed as the load dropped. The observations in Figs. 15 and 16 confirm the findings in Ref. [11]; matrix cracks occur first near the peak load and initiate delamination, which eventually determines the shear strength of a composite.

4. Conclusions

This study has presented the simultaneous application of the DIC and DVC techniques. The existing *in situ* test setup for the DVC analysis was modified to take pictures of the specimen surface for the DIC analysis. The modified test setup was demonstrated using the open-hole tension test. Image data for both the DIC and DVC computations were successfully collected. DIC results were useful for understanding the global response of the sample because the surface image data were collected over a wide area at every second. Although DVC results were limited only to seven load levels, the internal strain fields localized around the hole provided insightful information that could not be obtained only

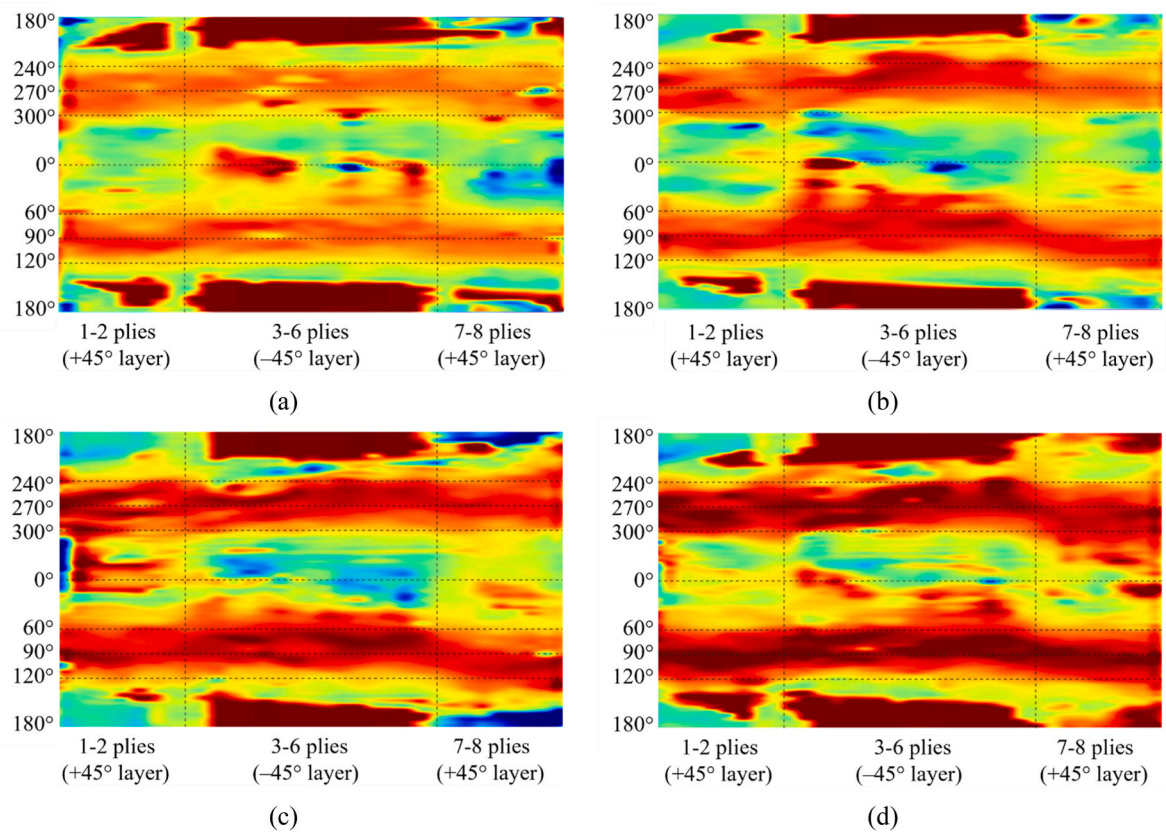

Fig. 13. Internal DVC strain fields around the hole along the thickness direction at (a) 60 MPa (b) 65 MPa (b) 70 MPa (d) 75 MPa.

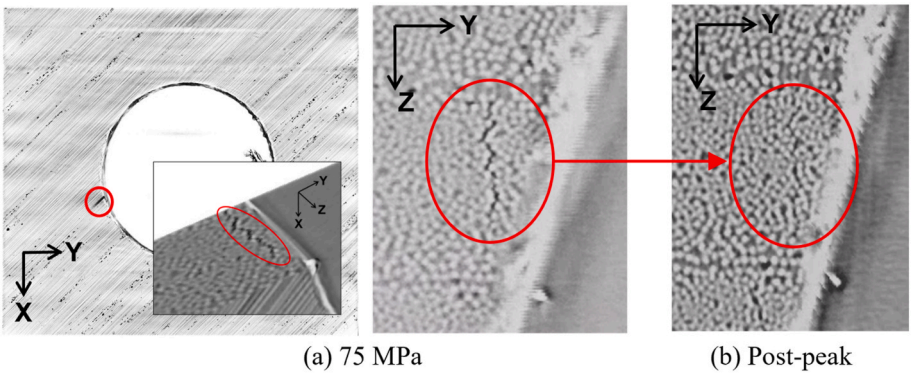

Fig. 14. Initial matrix crack in 4-ply (a) before and (b) after the peak.

from the DIC technique. The key findings and limitations of the study can be summarized as follows.

- DIC and DVC techniques were simultaneously applied for the first time to characterize the global and local behavior of a heterogenous material. Their synchronous application was demonstrated with the open-hole $[+45_2/-45_2]_S$ specimen. DIC provided the global strain field on the surface of the specimen and DVC revealed detailed strain distribution around the hole along the through-thickness direction.
- Owing to the DIC technique, the typical machine compliance issue of most miniature tensile stages is resolved. Supporting frames of the mini-size loading devices are often manufactured with X-ray penetrable materials not to distract its transmission. The machine compliance of such loading devices could be significant especially when a stiff material like carbon fiber-reinforced composites is tested. In that case, the machine compliance could be avoided by directly measuring the deformation of a sample instead of using a machine-provided cross-head displacement.
- The combination of computed tomography with the DIC and DVC techniques non-destructively yet comprehensively characterized the failure progression of the composite. The tomography found that the open-hole $[+45_2/-45_2]_S$ specimen failed just after transverse matrix cracks were initiated. No gradual failure progression in the matrix material was observed although DIC and DVC detected highly concentrated strains globally and locally before the peak stress was reached. This implies that the nonlinear shear response of the composite is mainly caused by the nonlinearity of the epoxy material and fiber orientation. Delamination immediately followed the initial transverse cracks, determining the shear strength of the sample. The overall failure process was similar with the findings reported in Ref. [11].

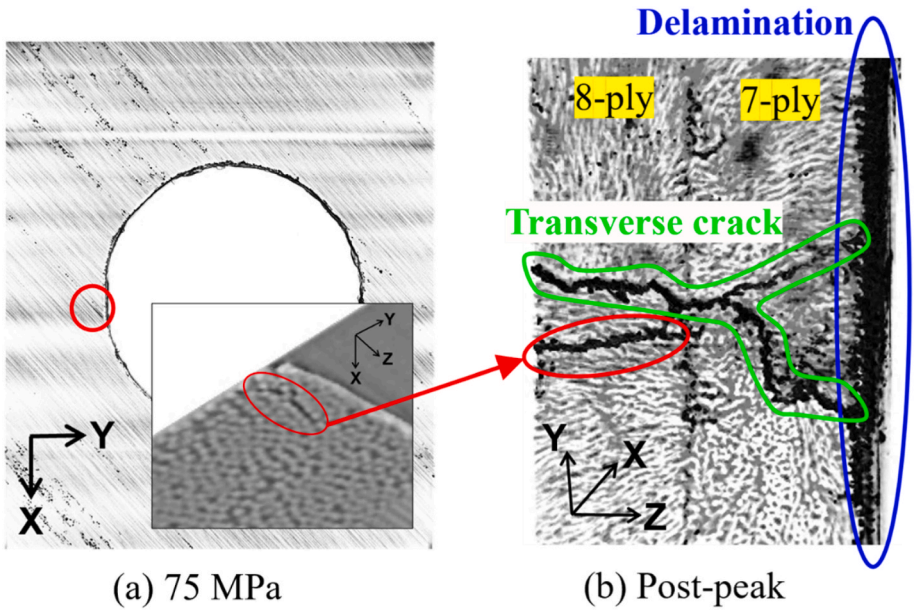

Fig. 15. Initial matrix crack in the 8-ply (a) before and (b) after the peak.

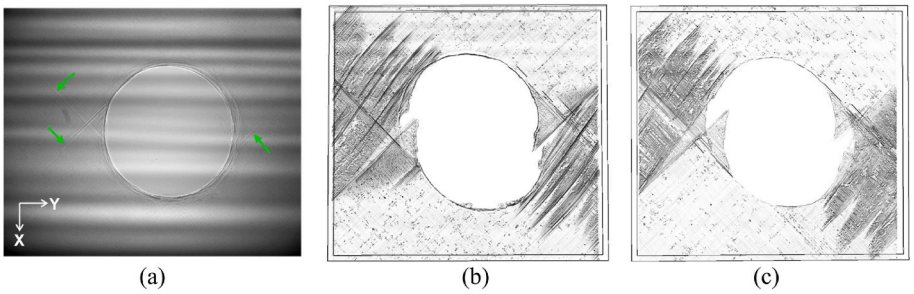

Fig. 16. Failure patterns (a) Projections from 1 to 8 plies at 77 MPa (b) Interface between 2 and 3 plies after the peak (c) Interface between 6 and 7 plies after the peak.

- Although the combination of CT, DIC, and DVC was technically successful, detailed failure mechanisms inside the OHT specimen were not characterized due to its rapid process. CT scans for the DVC analysis were still based on the conventional "stop-and-go" approach. This limitation may be overcome by employing a fast CT-scanning system [8] or experimenting with a different laminate gradually exhibiting progressive failure [14].

It is lastly noted here that the resolution of the DIC and DVC techniques in the presented study were 2.27 μm and 0.65 μm, respectively. Considering that the 0.65-μm resolution is sufficient to visualize most industry-grade carbon or glass fibers, the presented methodology is expected to provide unprecedented results that can truly validate multi-scale simulation models. The validation will also be supported by a global load-displacement curve having no machine compliance.

CRediT authorship contribution statement

Chaeyoung Hong: Visualization, Validation, Methodology, Investigation, Formal analysis, Data curation, Conceptualization. **Minsu Park:** Investigation, Data curation. **Wooseok Ji:** Writing – review & editing, Supervision, Project administration, Conceptualization.

Declaration of competing interest

The authors declare that they have no known competing financial interests or personal relationships that could have appeared to influence the work reported in this paper.

Acknowledgements

This work was supported by the National Research Foundation of Korea grant funded by the Korean Government (MSIT) (Grant No. 2021R1A2C2013545).

Data availability

Data will be made available on request.

References

[1] S.C. Garcea, Y. Wang, P.J. Withers, X-ray computed tomography of polymer composites, Compos. Sci. Technol. 156 (2018).
[2] J. Holmes, S. Sommacal, R. Das, Z. Stachurski, P. Compston, Digital image and volume correlation for deformation and damage characterization of fibre-reinforced composites: a review, Compos. Struct. 315 (2023).
[3] S. AhmadvashAghbash, et al., Translaminar fracture in (non-)hybrid thin-ply fibre-reinforced composites: an in-depth examination through a novel mini-compact tension specimen compatible with microscale 4D computed tomography, Compos. Appl. Sci. Manuf. 188 (2024).
[4] E. Van Vlierberghe, et al., Microstructural strain localisation phenomena in fibre-reinforced polymer composites: insights from nanoscale digital image correlation and finite element modelling, Compos. Sci. Technol. 258 (2024).
[5] S. Lee, E. Jo, W. Ji, Digital volume correlation technique for characterizing subsurface deformation behavior of a laminated composite, Compos. B Eng. 194 (2020).

[6] C. Hong, W. Ji, Complementary ex situ investigations of various fracture modes in a single-edge-notched symmetric cross-ply laminate subjected to tensile loading, Compos. Commun. 17 (2020).
[7] S. Lee, C. Hong, W. Ji, In situ micromechanical analysis of discontinuous fiber-reinforced composite material based on DVC strain and fiber orientation fields, Compos. B Eng. 247 (2022).
[8] E. Maire, C.L. Bourlot, J. Adrien, A. Mortensen, R. Mokso, 20 Hz X-ray tomography during an in situ tensile test, Int. J. Fract. 200 (2016).
[9] S.C. Garcea, I. Sinclair, S.M. Spearing, P.J. Withers, Mapping fibre failure in situ in carbon fibre reinforced polymers by fast synchrotron X-ray computed tomography, Compos. Sci. Technol. 149 (2017).
[10] Y. Wang, M.J. Emerson, K. Conradsen, A.B. Dahl, V.A. Dahl, E. Maire, P.J. Withers, Evolution of fibre deflection leading to kink-band formation in unidirectional glass fibre/epoxy composite under axial compression, Compos. Sci. Technol. 213 (2021).
[11] C. Hong, S. Lee, W. Ji, Shear strength determining mechanism of a +/-45 laminate under tensile loading, Compos. Struct. 326 (2023).
[12] X. Ni, R. Kopp, E. Kalfon-Cohen, C. Furtado, J. Lee, A. Arteiro, G. Borstnar, M. N. Mavrogordato, L. Helfen, I. Sinclair, S.M. Spearing, P.P. Camanho, B.L. Wardle, In situ synchrotron computed tomography study of nanoscale interlaminar reinforcement and thin-ply effects on damage progression in composite laminates, Composites, Part B 217 (2021).
[13] S. Rosini, M.N. Mavrogordato, O. Egorova, E.S. Matthews, S.E. Jackson, S. M. Spearing, I. Sinclair, In situ statistical measurement of local morphology in carbon-epoxy composites using synchrotron X-ray computed tomography, Composites Part A 125 (2019).
[14] E. Jo, S. Lee, C. Hong, W. Ji, In situ observation of interactive failure modes in a single-edge notched symmetric cross-ply laminate using synchrotron X-ray tomography, Compos. Appl. Sci. Manuf. 128 (2020).
[15] X. Li, J. Ge, B. Zhang, X. Liu, L. Wang, S. Liu, J. Liang, X-ray computed tomography study of compressive failure in a notched unidirectional glass fibre-reinforced composites, Polym. Test. 130 (2024).
[16] F. Rojas-Sanchez, A.M. Waas, Characterization of damage initiation in fiber reinforced composites from high resolution experimental data, Compos. Appl. Sci. Manuf. 173 (2023).
[17] J.Y. Buffiere, E. Maire, J. Adrien, J.P. Masse, E. Boller, In situ experiments with X-ray tomography: an attractive tool for experimental mechanics, Exp. Mech. 50 (3) (2010) 289–305.
[18] H. Rolland, N. Saintier, G. Robert, Damage mechanisms in short glass fibre reinforced thermoplastic during in situ microtomography tensile tests, Composites, Part B 90 (2016).
[19] H.A. Bale, et al., Real-time quantitative imaging of failure events in materials under load at temperatures above 1,600°C, Nat. Mater. 12 (2013) 40–46.
[20] CT5000 Tensile Stage, Deben, United Kingdom.
[21] S. Lee, W. Ji, DVC analysis of a polymer material subjected to tensile loading with synchrotron radiation tomography, Polym. Test. 81 (2020).
[22] GOM GmbH, ARAMIS v6.3 User Manual, 2005. Germany.